5

Geophysical methods

J.-L. Mari

Studies conducted at the Hydrogeological Experimental Site (HES) focus mainly on the Dogger Aquifer. Conventional hydrogeological surveys have investigated the site, which was also subjected to geophysical investigations both from the surface and in wells. These studies include conventional hydrological surveys and geophysical investigations, both from the surface and in wells. On the site, 35 boreholes have been drilled (Fig. 1).

In 2004, 3D seismic data were recorded to obtain a 3D velocity model in depth. A vertical seismic profile (VSP) was recorded in borehole C1 to perform the time-to-depth conversion of the seismic block. An acoustic tool was run in boreholes C1, MP5, MP6, M08, and M09 to record full waveform acoustic data and compute velocity logs used as constraints for converting seismic amplitudes in pseudo-velocities during the inversion process. The resulting 3D seismic pseudo-velocity block revealed three main high-porosity, presumably water-producing layers, at depths of 35-40, 85-87, and 110-115 m that were identified as karstic levels.

Multi-borehole logging investigations were carried out at the HES site (Audouin et al., 2008). To confirm the presence of karstic layers, both acoustic and seismic borehole data were collected from several boreholes. In the low-frequency range (10–150 Hz), Vertical Seismic Profile (VSP) data were acquired using a hydrophone sensor, which is particularly sensitive to Stoneley waves — commonly used to detect subsurface discontinuities such as fractures or faults. In the high-frequency range (1–20 kHz), full waveform acoustic logs were recorded to provide a detailed characterization of the formations.

DOI: https://doi.org/10.1051/978-2-7598-3934-6.c005

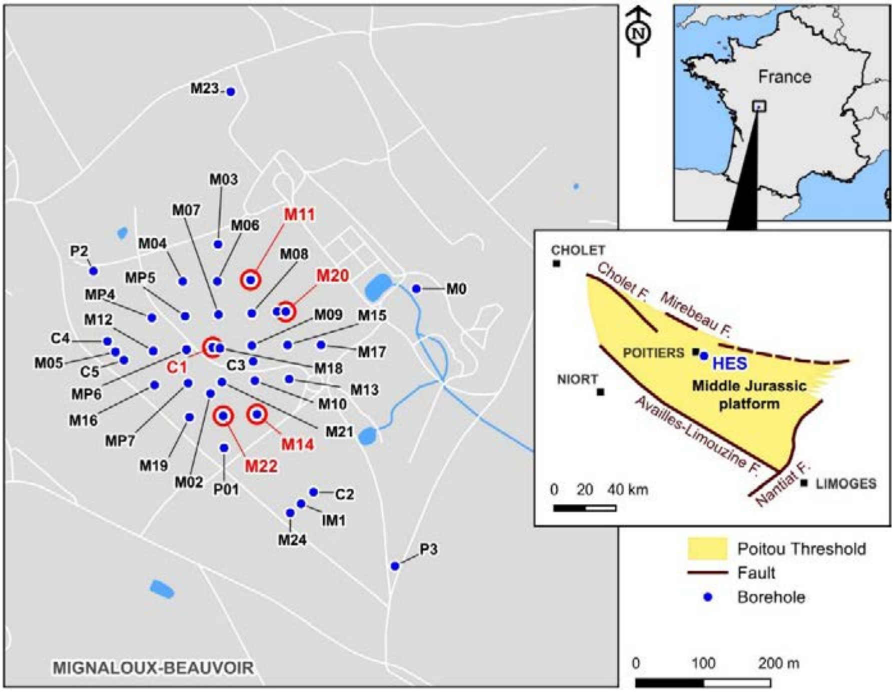

Figure 1 *The hydrological experimental site and borehole locations. Boreholes C1, M11, M14, M20, and M22 (indicated by red circles) were selected for seismic and stratigraphic characterization of karstogenic horizons.*

In 2014, the acoustic tool was rerun in boreholes C1, MP5, MP6, MP7, M03, M05, M11, M13, M14, M20, and M22. In 2015, VSP with hydrophones was recorded in boreholes C1, M03, M04, M07, M11, M20, MP6, and MP7. In each borehole, in addition to VSP recording, ambient noise measurements were done.

Boreholes M11, M14, M20, and M22 were selected for seismic and stratigraphic characterization of karstogenic horizons (Gaillard et al., 2024).

The chapter presents an overview of the field experiments conducted using mainly seismic and acoustic methods and shows their relative contribution to the understanding of the experimental site. Boreholes C1 and M20 are selected to illustrate the VSP method. Boreholes C1, M11, M14, M20, and M22 are selected to illustrate the acoustic method.

5.1 Seismic and acoustic methods

The 3D survey was designed to obtain a 3D block based on records of low amounts of data [1, 2, 3]. The complete survey is composed of 20 receiver lines (the in-line direction) with a 15 m lag distance between adjacent lines (Fig. 2a), each line being composed of 48 single geophones with 5 m spacing between adjacent geophones. For each receiver line investigated, direct and reverse shots (source in line with the receiver line) were recorded (Fig. 2b top), as well as cross-line shots fired at distances of 40, 50, and 60 m perpendicular to the receiver line (Fig. 2b bottom). Processing the data from in-line direct and reverse shots gathers the results in a vertical section of 240 m in-line extension (the blue arrow, in

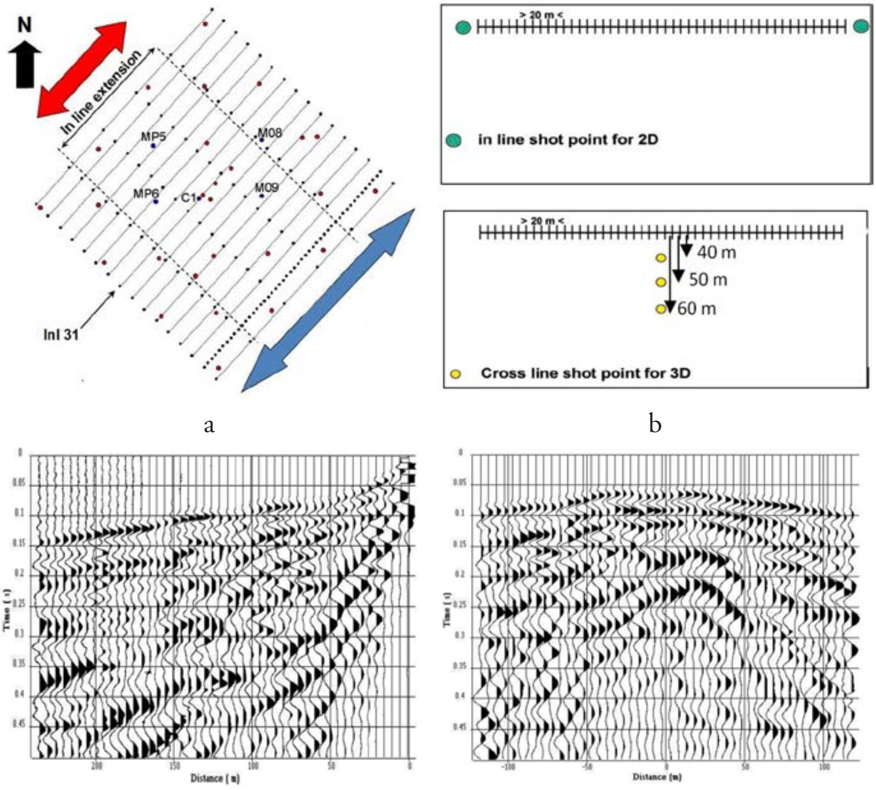

a b

c d

Figure 2 *Seismic spreads and field implementation of seismic lines. Modified after Mari et al. 2008 and 2011. (a) Seismic line implementation: the distance between two adjacent lines is 15 m; red points indicate well locations. (b) Seismic spreads: A direct shot and a reverse shot are fired in line to obtain 2D seismic images (top). Several shots are fired cross-line to obtain 3D seismic images (bottom). (c) Example of in-line shot gather, d) Example of cross-line shot gather with 60 m of lateral offset.*

Fig. 2a) with an in-line extension of 240 m, while a cross-line shot gathers results in a vertical section of only 120 m extension along the in-line direction (the red arrow on the location map of seismic lines, in Fig. 2a). Figures 2c and 2d show examples of an in-line shot (Fig. 2c) and a cross-line shot with a lateral offset of 60 m, respectively (Fig. 2d).

The range of offsets was selected to optimize the quality of the seismic image over the reservoir depth interval, i.e., between 40 m and 130 m. A 40 m minimum offset distance was chosen to reduce the influence of the surface waves. The time-sampling interval was 0.25 ms, and the recording length was 0.5 s.

To perform the time-to-depth conversion of the seismic block, a vertical seismic profile (VSP) was recorded in borehole C1, using a vertical geophone as a borehole sensor. The source is a light seismic source (weight dropper). The sensor was clamped in the borehole, in the 25–120 m depth interval, with a depth sampling interval of 2.5 m. The time-sampling interval was 0.25 ms, and the recording length was 0.5 s. The VSP record is shown in Figure 3a. The vertical axis represents the recording time, and the horizontal axis represents the depth locations of the borehole sensor. The first arrival wave is the down-going P-wave. The picking of its arrival times at the different sensor locations is used to compute both the time vs depth law and the Rms-velocity log (Fig. 3b).

Acoustic data were recorded in borehole C1. The acoustic probe (Gaudiani, 1979) is a flexible monopole tool holding a source as a magnetostrictive transducer and a pair of far receivers (3 and 3.25 m offsets beneath the source). The acoustic data were recorded in the 1–20 kHz frequency band. The sampling intervals are 5 µs in time and 5 cm in depth. In a vertical well, monopole tools can enable the recording of five propagation modes including: refracted compression waves (P), refracted shear waves (S, only in fast formations VS > VP fluid, P-wave velocity of the borehole fluid), fluid waves (F), and two dispersive guided modes as pseudo-Rayleigh waves (in fast formations), and Stoneley waves (ST). The acoustic logs associated with the different waves are very high-resolution logs and can be compared with core measurements. The acoustic logs currently obtained for each type of wave are velocity or slowness logs, frequency, and attenuation logs. Full waveform acoustic measurements can be represented as constant-offset sections. A constant-offset section is a set of acoustic records represented as a function of depth and obtained with a fixed source-to-receiver distance. Figure 3c shows the 3m constant-offset acoustic section, with the identification of the refracted P-wave (P), the converted refracted S-wave (S), and the Stoneley wave. One can notice a strong attenuation of the different waves (P, S, Stoneley) in the 50–53 m depth interval, which corresponds to a karstic level (Mari & Porel, 2015).

Figure 3d shows the velocity logs computed from the picked arrival times of the refracted P-wave at the two receivers of the acoustic probe. The acoustic velocity log (Fig. 3d left) has been filtered (Fig. 3d right) to have a vertical resolution compatible with the seismic resolution to invert the seismic data to recover seismic velocities from seismic amplitudes.

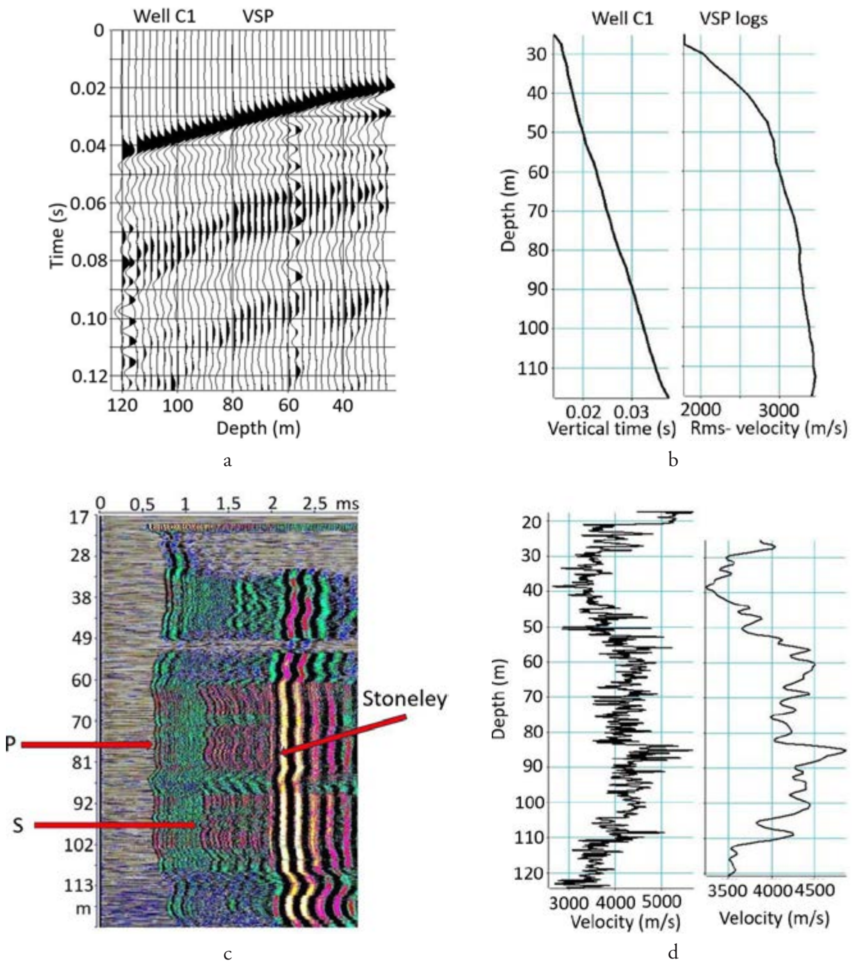

a b

c d

Figure 3 *Vertical Seismic Profile (VSP) and acoustic logging at well C1. Modified after Mari et al. 2009, Delay et al., 2022. (a) VSP section. (b) Time vs depth law and Rms-velocity log. (c) Acoustic section; vertical axis: depth in m, horizontal axis: time in ms. (d) acoustic velocity logs.*

Combined analyses of geophysical and hydrogeological data can be conducted locally at wells or at a larger scale using 3D seismic data. These studies are done for the purpose of detecting water-producing levels at wells and establishing a probable network of karst conduits. An integrated approach based on tracer tests and geophysical data has been developed for identifying effective three-dimensional (3D) discrete karst conduit networks (3D velocity block, Fig. 5) (Bodin, Porel et al., 2022).

5.2 3D seismic imaging

The processing sequence has been described in detail in several publications (Mari & Porel 2008, 2018, and Mari & Delay, 2011), so it is only briefly explained here. Each shot point was processed independently (both in the cross-line direction and in the in-line direction) to obtain a single-fold section with a sampling interval of 2.5 m (half the distance between two adjacent geophones) in the in-line direction. The processing of an in-line direct and reverse shot gather has made it possible to obtain a single-fold section with an in-line extension of 240 m (indicated by a blue arrow on the seismic line map, Fig. 2a) while a cross-line shot gather has provided a single-fold section with an in-line extension of 120 m (indicated by a red arrow on the seismic lines map, Fig. 2a).

A 3D refraction seismic tomography (Mari & Mendes, 2012) was done to map the irregular shape of the top of the karstic reservoir and to obtain static corrections (obtained by inversion tomography after geostatistical analysis, see appendix) and a velocity model of the overburden. To add information to the inversion procedure, we used in-line and cross-line cross shots simultaneously, with an offset of 60 m. The shots were selected to ensure that the refracted wave was the first arrival wave, regardless of the source-receiver distance. The picked times of the first seismic arrivals for all shots (in-line and cross-line shots), and both the depth map of the top of the reservoir and the velocity model obtained by the Plus–Minus (Mari & Mendes, 2019) method were used as input data for the tomographic inversion procedure.

The processing sequence (Mari & Porel, 2008, 2018) includes amplitude recovery, deconvolution, wave separation, static corrections (obtained by inversion tomography) and normal move-out (NMO) corrections, using the Vrms velocity log obtained from VSP recorded in borehole C1 (Fig. 3a and 3b). The VSP time versus depth law (Fig. 3b) was also used to convert the time sections into depth sections with a 0.5 m depth sampling interval. The single-fold depth sections were merged to create the 3D block. The width of the block in the in-line direction is 240 m, and 300 m in the cross-line direction. In the in-line direction, the abscissa zero indicates the location of the source line. The abscissa of the reflecting points ranges between -120 m and 120 m in the in-line direction. The distance between the two reflecting points is 2.5 m. In the cross-line direction, the distance between two reflecting points is 5 m. The depth sections were deconvolved to increase the vertical resolution. They were then integrated to transform a 3D amplitude block into a pseudo-velocity block, using velocity functions (filtered sonic logs obtained by full waveform acoustic logging at boreholes C1 (Fig. 3d), MP5, MP6, M08, and M09 as constraints. The pseudo-velocity sections of the 3D block thus obtained were merged with those obtained by refraction tomography to create a 3D extended velocity model from the surface. Figure 4 shows the in-line 31 pseudo-velocity section. The upper part of the figure shows the velocity distribution obtained by refraction tomography. The seismic section clearly shows nearly horizontal stratifications with strong lateral variations of seismic velocities. Figure 5 shows both the 3D seismic velocity model from 35 to 130 m below the ground surface and the

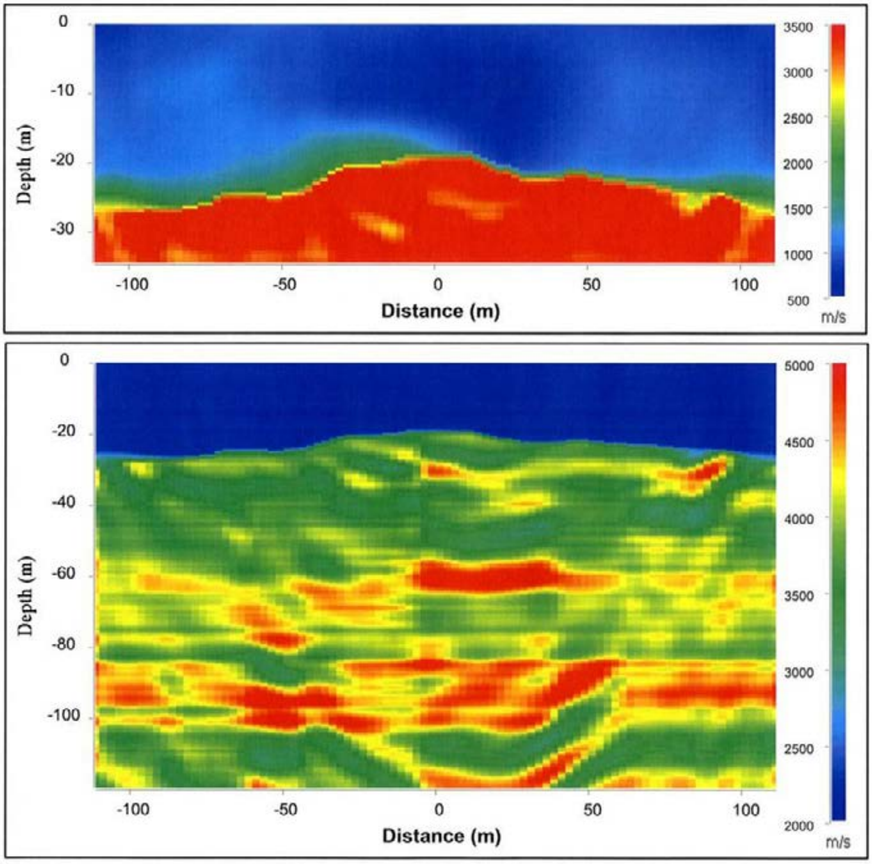

Figure 4 *3D seismic imaging: in-line 31 pseudo-velocity section (upper part: zoom of 0 to 35 m depth interval). Modified after Mari et al., 2018.*

seismic velocity logs extracted from the 3D block at borehole locations M11, M14, M20, and M22. We notice a strong velocity decrease in the 80–90 m depth interval.

To quantify porosity variations within this aquifer, the seismic interval velocities were first converted into resistivity values. For this purpose, the empirical relationship between seismic velocity and resistivity proposed by Faust [1953] was used (Mari, Porel & Bourbiaux, 2009). At each well where a long normal log Rt (Chapellier, 2001b) has been recorded, an interval velocity log V was extracted from the 3D block. The two sets of data (resistivity Rt and seismic velocity V) were combined to compute empirical Faust's laws which were used to transform the 3D pseudo-velocity block into a 3D pseudo resistivity block, using resistivity functions (resistivity logs Rt recorded at 12 wells MP4, MP5, MP6, M11, M13, M14, M18, M21, M04, M07, M08 and M09) as constraints. Figure 6a shows comparisons between resistivity logs Rt from logging and resistivity logs Rt-seis from seismic velocity at boreholes M11 and M14. Figure 6b shows the resistivity logs Rt-seis at boreholes M11, M14, M20, and M22, which highlight a strong resistivity decrease in the 80–90 m depth interval. Resistivity values were then converted into porosity values, using Archie's law (1942). The resulting 3D seismic pseudo-porosity block (Fig. 7a) revealed three high-porosity layers, at depths of 35 to 55 m, 85 to 87 m,

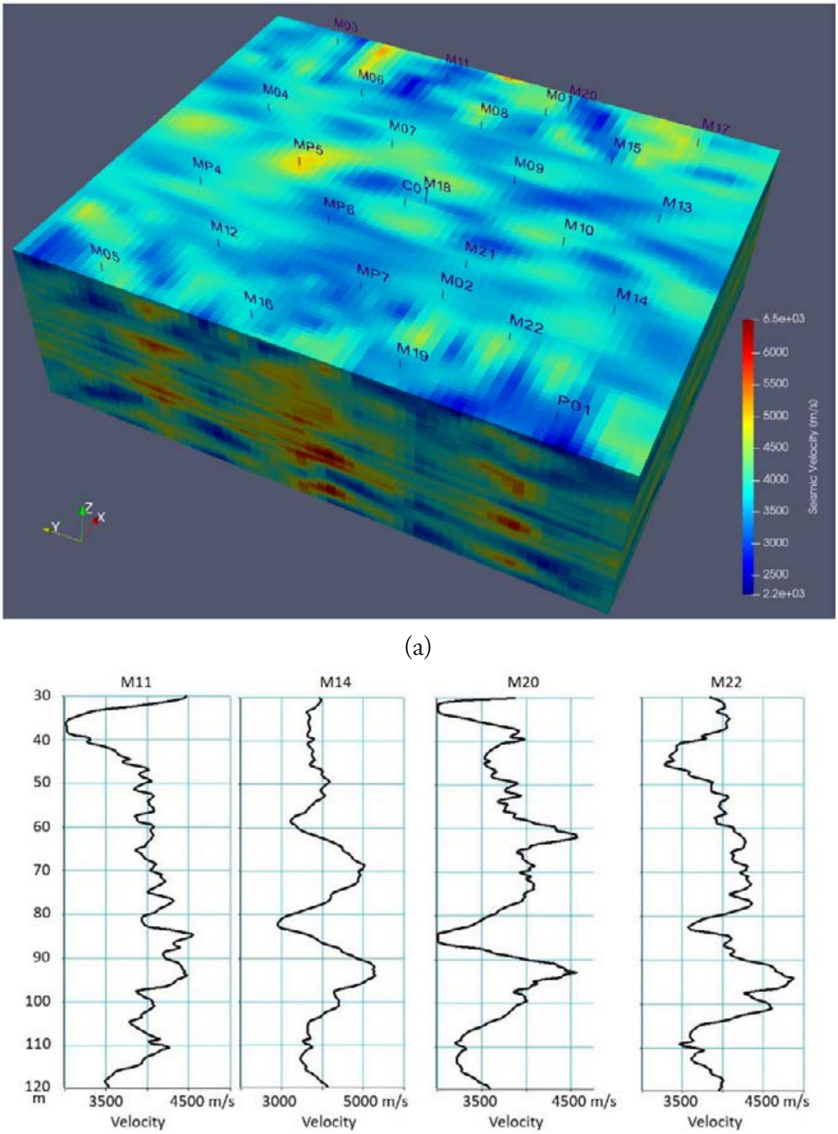

(a)

(b)

Figure 5 *3D seismic imaging. (a) 3D seismic velocity model from 35 to 130 m below the ground surface. Modified after Bodin et al. 2022. (b) Velocity log extracted from the 3D block at borehole locations: M11, M14, M20, and M22.*

and 110 to 115 m. The 85 to 87 m layer is the most porous, with porosities higher than 30 %, which represents the karstic part of the reservoir. Figure 7b shows the seismic pseudo-porosity logs extracted from the 3D block at boreholes M11, M14, M20, and M22.

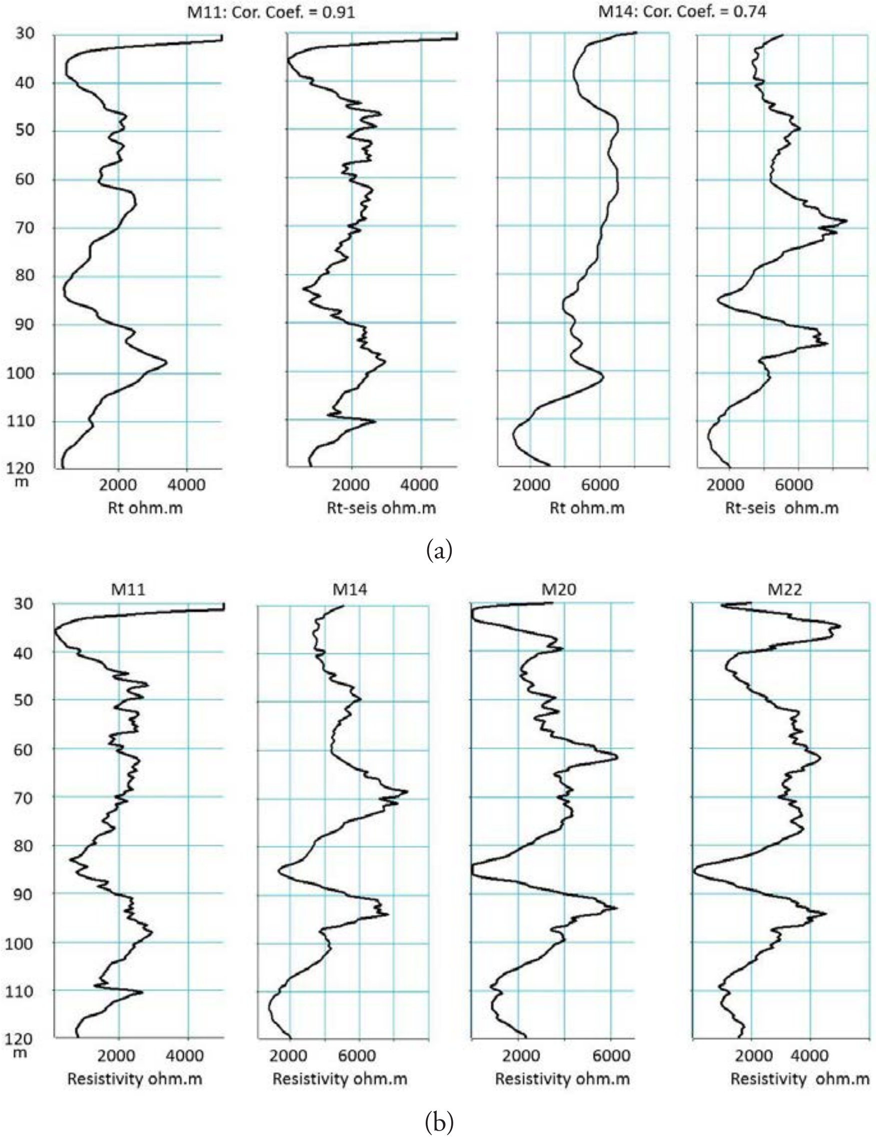

(a)

(b)

Figure 6 *Resistivity log from the 3D velocity block. (a) Comparison between the resistivity log from logging and resistivity log from seismic velocity at boreholes M11 and M14. (b) Resistivity log from seismic velocity at boreholes M11, M14, M20, and M22.*

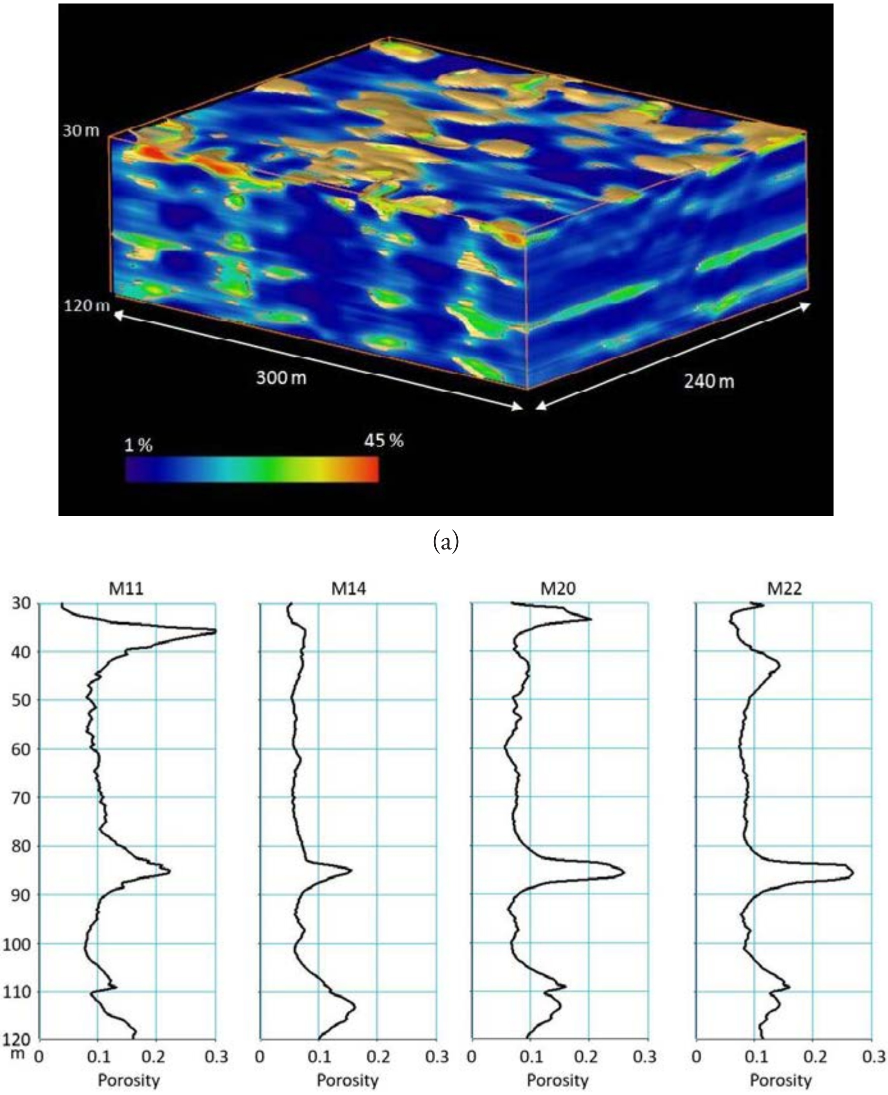

(a)

(b)

Figure 7 *3D porosity block. (a) 3D Seismic porosity block in the 30–120 m depth interval. Modified after Mari et al. 2009, Delay et al., 2022. (b) Seismic porosity logs extracted from the 3D porosity block at boreholes M11, M14, M20, and M22.*

Figure 8a shows the distribution of porous bodies in the 80 to 120 m depth intervals. Figure 8b shows the porosity distribution (A) and karstic body extension (B) in the central part of the 3D block.

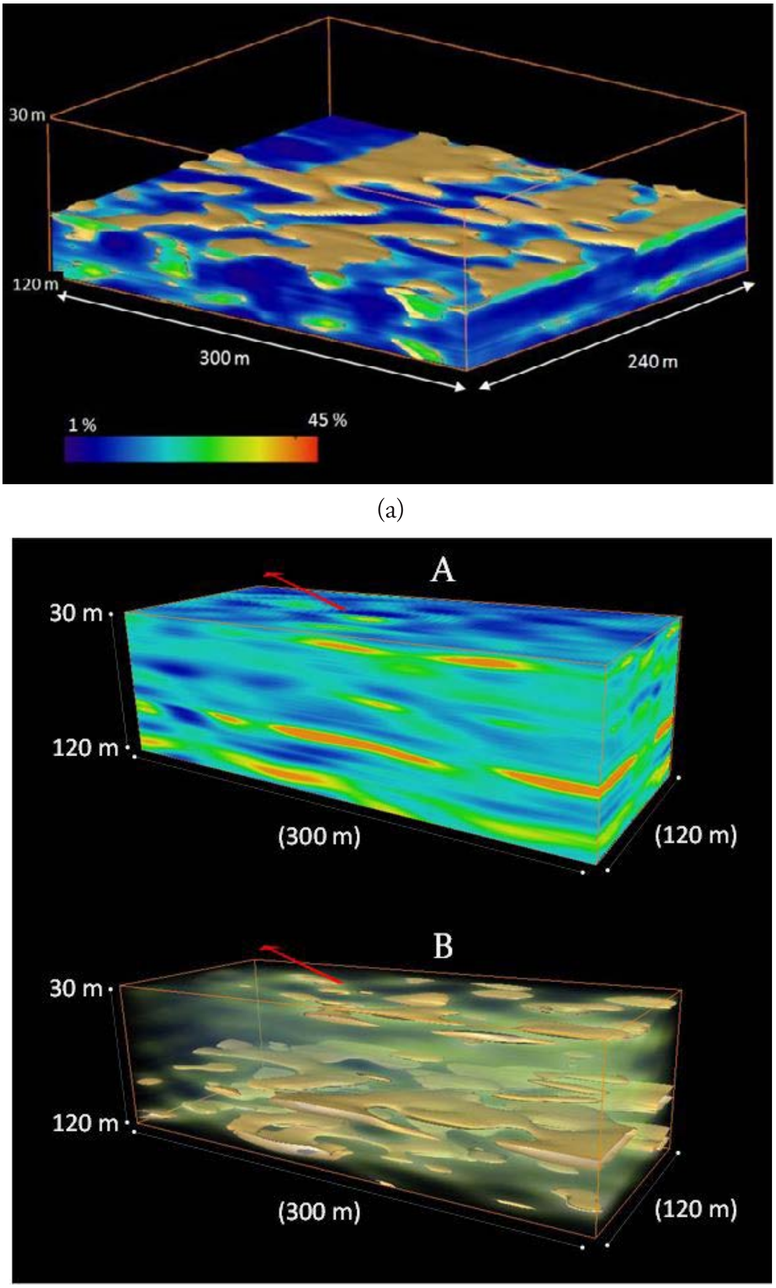

(a)

(b)

Figure 8 *3D Seismic porosity block. (a) Porosity distribution in the 80–120 m depth interval. Modified after Mari et al. 2009, Delay et al., 2022. (b) b: Porosity distribution (A) and karstic body extension (B) in the central part of the 3D block. Poitiers University document.*

5.3 Full waveform acoustic logging

Processing based on Singular Value Decomposition (Mari & Porel, 2018) was conducted independently on the two offset sections (3 m and 3.25 m) recorded with the acoustic tool. The processing is done to extract the wavelets associated with the different waves (refracted P-wave, converted refracted S-wave, and Stoneley wave) on the two sections. For a wave type (for example, the refracted P-wave), the correlation of the two wavelets observed at offsets 3 m and 3.25 m enables the simultaneous computation of the formation velocity V, the correlation coefficient between the wavelets, and the amplitude of each wavelet. The amplitude measurements can be used to compute amplitude ratio and attenuation logs, which can be expressed in dB and dB/m. Figure 9 shows the velocity, correlation, and attenuation logs computed from acoustic sections (Fig. 2c) recorded in borehole C1. In the 50–53 m depth interval, which corresponds to a karstic level, we notice a significant decrease in velocity, a very low correlation coefficient, and strong attenuation. The same observations can be made in the 85–90 m depth interval on the correlation and attenuation logs.

SVD processing leads to the calculation of a specific attribute used to detect karstic levels. The attribute, called Karstic Index, is the product of three normalized terms:

- a velocity term: $CV = 1 - (V/V_{max})$. The lower the velocity, the higher the velocity term. In karstic zones, a high CV coefficient is observed;
- an amplitude ratio term: $CAR = 1 - (AR/AR_{max})$, where AR is amplitude ratio. In karstic zones, a high CAR coefficient is observed;

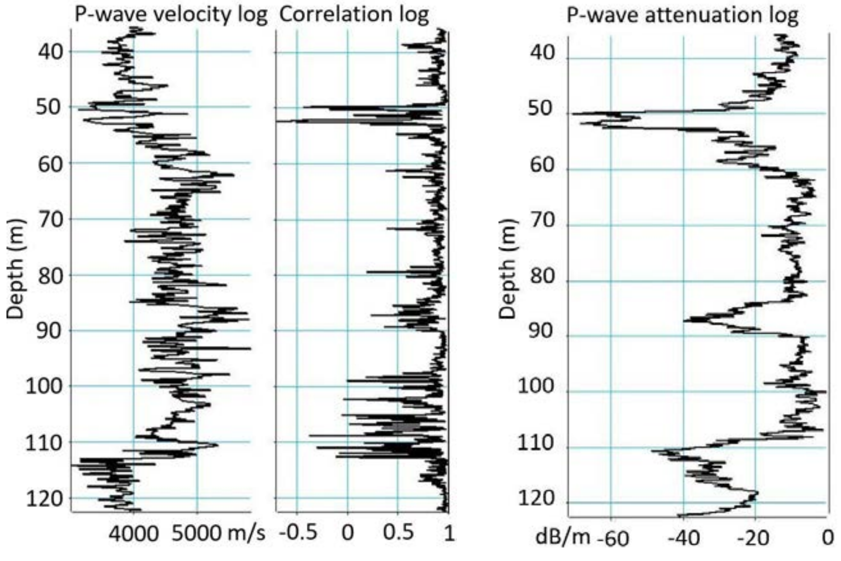

(a) (b)

Figure 9 *FWAL at well C1: Refracted P-waves. (**a**) Velocity log and its associated correlation coefficient log. (**b**) Attenuation log. Modified after Delay et al., 2022.*

- a correlation term: CCor = 1 – (Cor/Cor_{max}), with Cor being the correlation coefficient between two normalized wavelets. In karstic zones, a high CCor coefficient is observed.

Figure 10a shows the 3m constant offset sections recorded in boreholes M11, M14, M20, and M22. On the acoustic sections, refracted P-waves appear in the 0.5–1.2 ms time interval, converted refracted S-waves and pseudo-Rayleigh waves

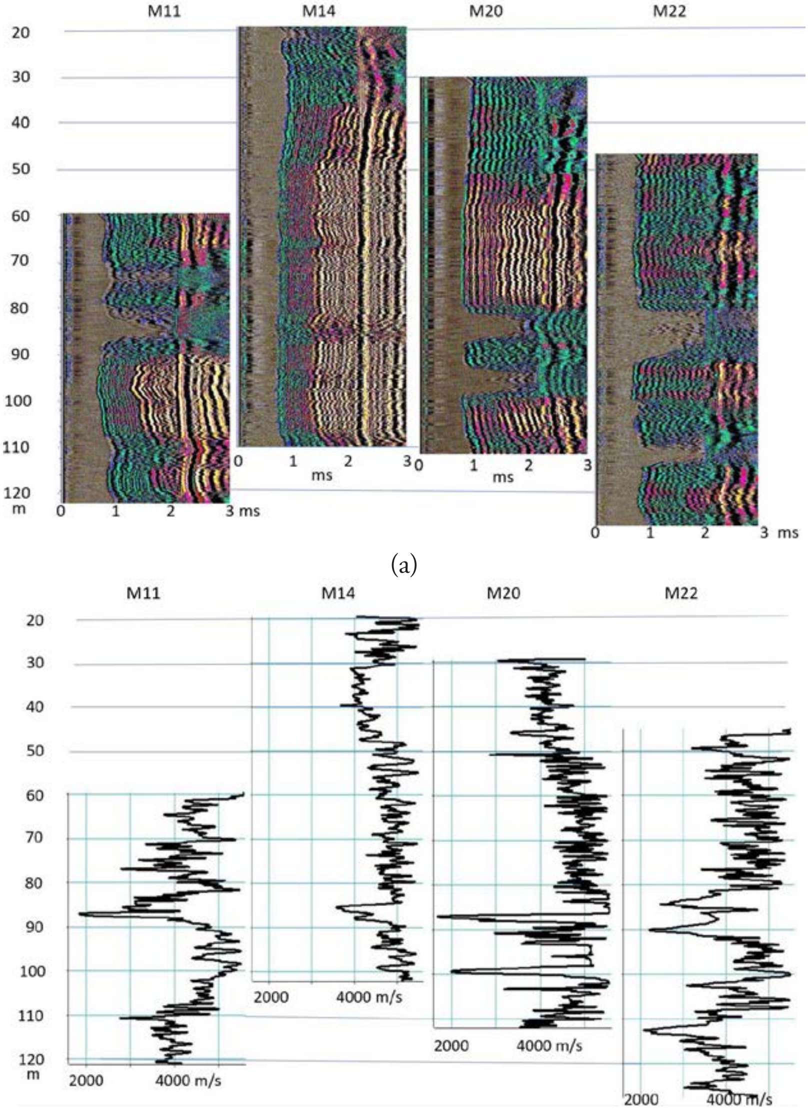

(a)

(b)

Figure 10 *FWAL at boreholes M11, M14, M20, and M22: (a) acoustic sections, (b) P-wave velocity logs.*

in the 1.2- 2 ms time interval, and Stoneley waves in the 2–3 ms time interval. Velocity, amplitude ratio, and karstic index logs are shown in Figures 10b, 11a, 11b, respectively.

The acoustic section recorded in borehole M11 shows:

- the 60–72 m depth interval, all acoustic waves (refracted P-wave, converted refracted S-wave, and Stoneley wave) are visible with high amplitude, indicating a compact formation;
- the 72–75 m depth interval, the refracted P-wave has low amplitude, the S-wave cannot be observed. Stoneley waves are strongly attenuated, and fluid waves appear;
- the 75–80 m depth interval is a homogenous formation;
- the 80–90 m depth interval, body waves (P and S) and Stoneley waves are not present. Only fluid waves are present, indicating a karstic level;
- the 90–120 m depth interval corresponds to a homogeneous formation, all acoustic waves (refracted P-wave, converted refracted S-wave, and Stoneley wave) are visible and of high amplitude, indicating a compact formation. However, in the 110–115 m depth interval, we notice a slight attenuation of the different waves (Fig.11a) and the presence of a fluid wave.

The acoustic section recorded in borehole M14 shows:

- the 22–38 m depth interval, where only refracted P-waves and Stoneley waves are recorded, indicating a slow formation. We note the presence of fluid waves;
- the 38–110 m depth interval of homogeneous profile with a high signal-to-noise ratio; all acoustic waves (refracted P-wave, converted refracted S-wave, and Stoneley wave) are visible and of high amplitude, indicating a compact formation. No fluid waves are visible. However, in the 85–88 m depth interval, we note a very weak attenuation of the various waves, which is confirmed by small decreases of both the P-wave velocity log and the amplitude log (Fig. 10b and 11a).

Analysis of the acoustic data (Fig. 11b) shows a small but significant increase of karstic body indicators in the 85–90 m depth interval, suggesting the presence of a karstic feature filled with sediments such as shale. However, no flow is present.

The acoustic section recorded in borehole M20 shows:

- in the 30–58 m depth interval, an acoustically slow formation where only refracted P-waves and Stoneley waves propagate;
- in the 58–80 m depth interval, an acoustically fast formation where refracted P-waves, converted refracted S-waves and Stoneley waves propagate, indicating a compact geological formation;
- A karstic unit in the 80–100 m depth interval, characterized by strong attenuation of refracted P-waves (Fig. 11a) and Stoneley waves. In the interval, we can infer the presence of fluid waves, indicating the presence of flow;
- in the 100–110 m depth interval, an acoustically fast formation where refracted P-waves, converted refracted S-waves and Stoneley waves propagate, indicating a compact geological formation.

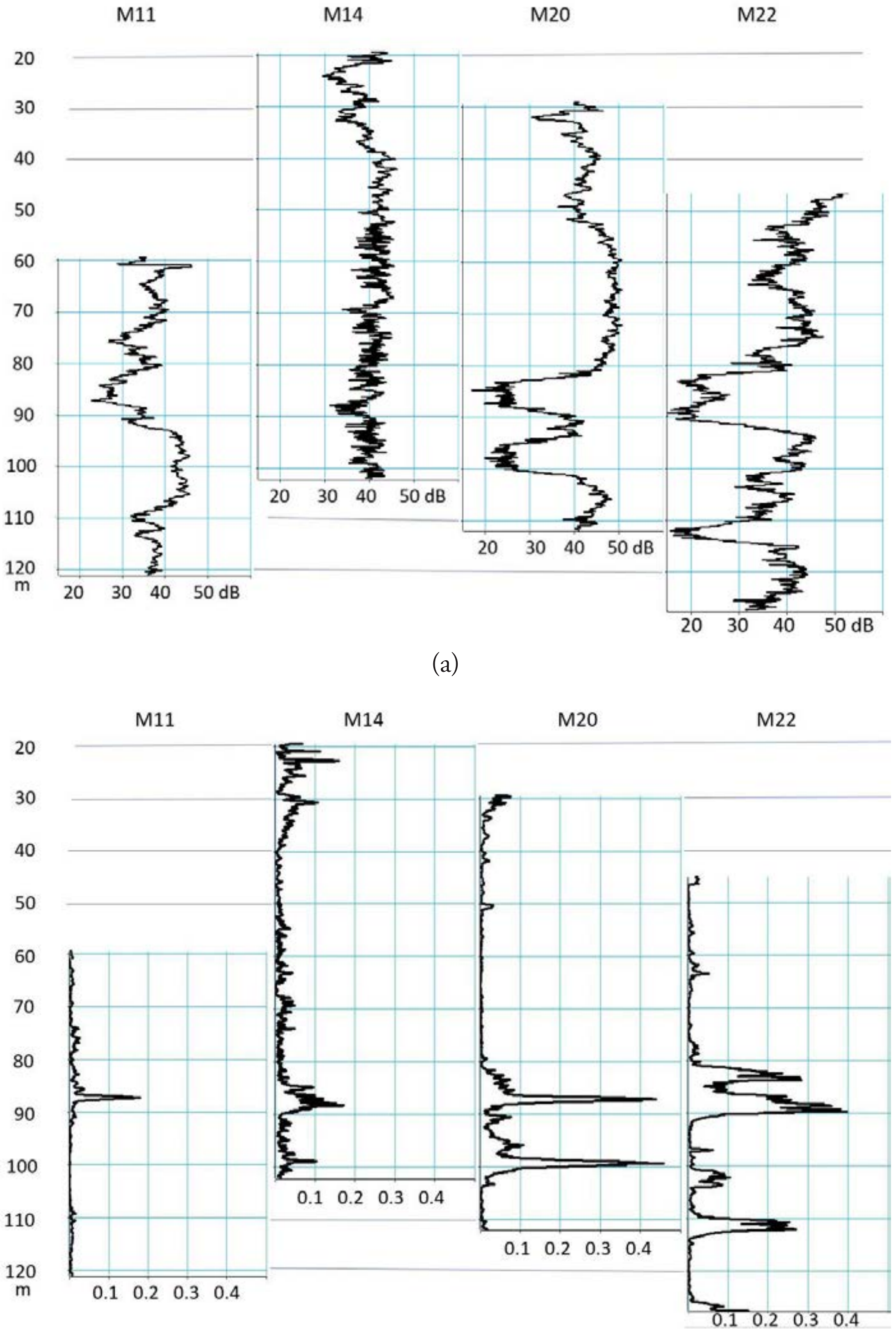

(a)

(b)

Figure 11 *Acoustic logs in boreholes M11, M14, M20, and M22: (a) amplitude ratio logs, (b) karstic Index logs.*

The acoustic logs (Fig. 10b, 11a and 11b) clearly show that the karstic unit is composed of two karstic levels at depths of 82–87 m and 93–100 m.

The acoustic section recorded in borehole M22 shows:

- in the 45–80 m depth interval, an acoustically homogeneous formation. Refracted P-waves and Stoneley waves are clearly visible. It is more difficult to identify the converted refracted S-wave;
- a karstic unit in the 80–90 m depth interval, characterized by strong attenuation of refracted P-waves (Fig. 11a) and Stoneley waves. In the interval, we can infer the presence of fluid waves, indicating the presence of flow;
- in the 90–110 m depth interval, an acoustically homogeneous formation;
- a second karstic unit in the 110–115 m depth interval, characterized by strong attenuation of refracted P-waves (Fig. 11a) and Stoneley waves. In the interval, we can infer the presence of fluid waves, indicating the presence of flow;
- in the 115–125 m depth interval, an acoustically homogeneous formation.

The amplitude ratio and karstic index logs (Fig. 11a and 11b) clearly show two karstic levels at depth intervals of 80–90 m and 110–115 m.

In addition to the analysis of the acoustic sections, acoustic logs are used to identify the karstic levels. A high karstic index value (Fig. 11b) provides an accurate location of a karstic layer. Integration in depth of the karstic index from the bottom to the top of the borehole is computed to mimic a flowmeter (Mari & Porel, 2015). Acoustic flowmeters are shown in Figure 12.

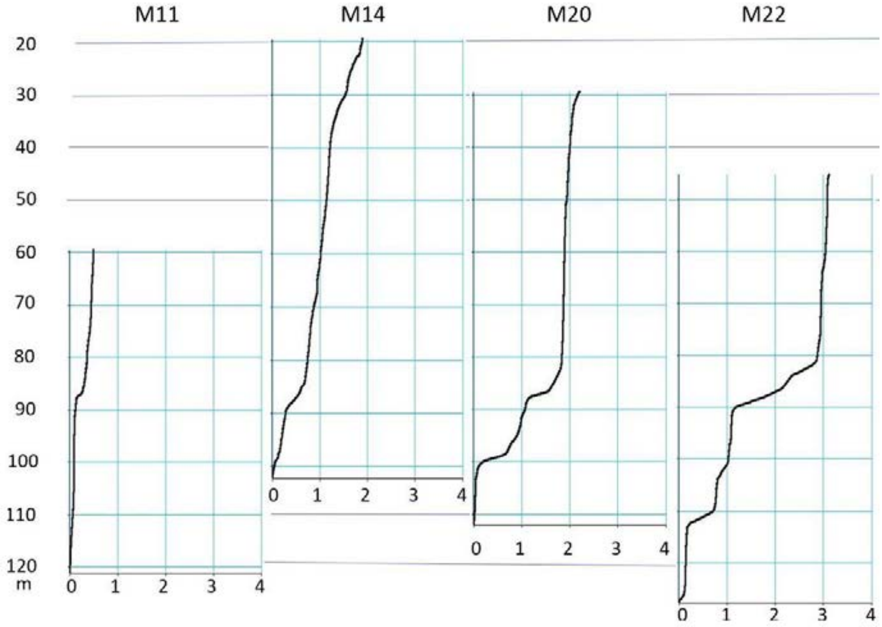

Figure 12 *Acoustic logs in boreholes M11, M14, M20, and M22: acoustic flow logs.*

5.4 Vertical seismic profiles versus full waveform acoustic logging

VSP acquisition was also done using a hydrophone as a borehole sensor and a light-weight dropper as a source. The depth sampling interval is 2.5 m. Figure 13 shows the VSPs recorded in boreholes C1 and M20. The VSPs were highly corrupted by Stoneley waves. The conversion of down-going P-waves (blue arrow in VSP

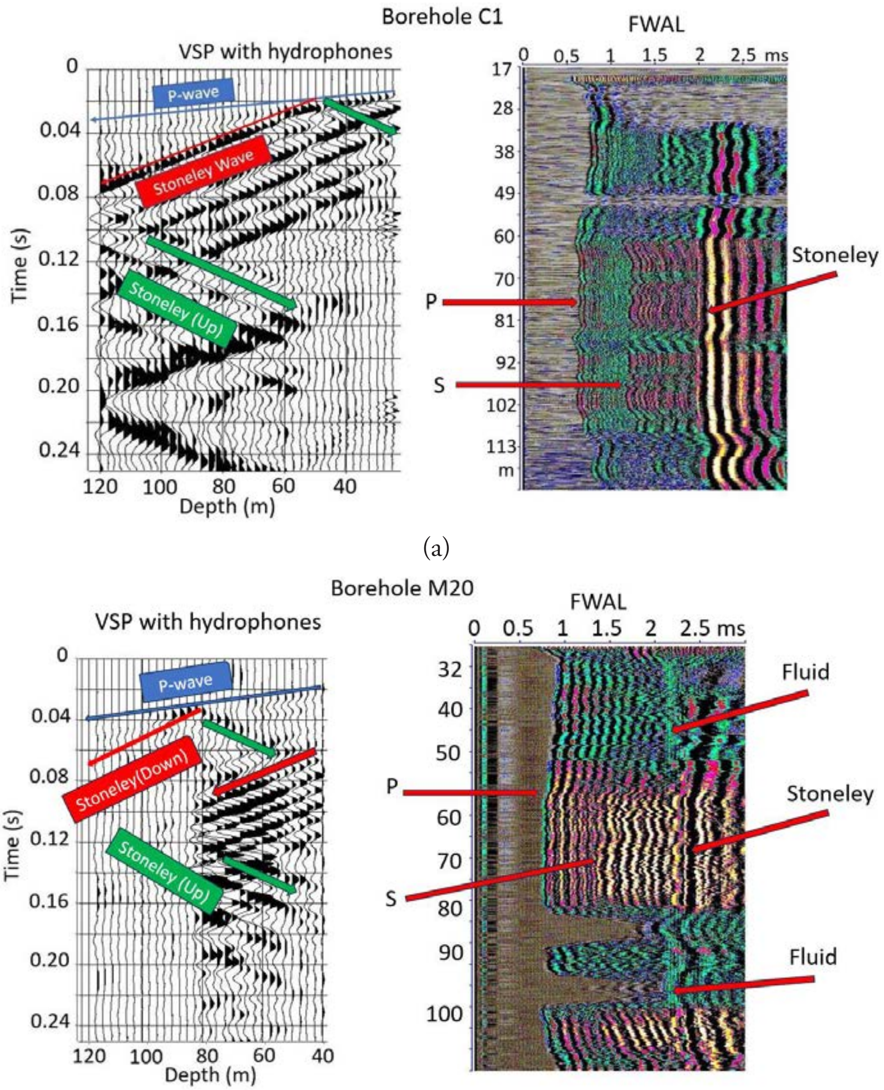

(a)

(b)

Figure 13 *Comparison between VSP and acoustic data at boreholes C1 (a) and M20 (b).*

sections) into down-going and up-going Stoneley waves was observed at the level of the karstic bodies. This phenomenon occurs in highly permeable formations. On the VSP sections, the down-going P-wave is identified by a blue arrow, the down-going Stoneley waves by red arrows, and the up-going Stoneley waves by green arrows.

On VSP recorded at borehole C1, the phenomenon of conversion of a down-going P-wave into a down-going Stoneley wave can be observed at a depth of 50 m (Fig. 13a, left). It is more difficult to identify the converted upgoing Stoneley wave. Indeed, it can be noted that the down-going P-wave is highly attenuated at the same depth. The acoustic section (Fig. 13a, right) clearly shows the karstic level where the conversion phenomenon occurs.

On VSP recorded at borehole M20, the conversion of the down-going P-wave into down-going and up-going Stoneley waves is clearly visible at a depth of 80 m (Fig. 13b, left), which corresponds to the top of karstic layers identified on the acoustic section (Fig. 13b, right).

On the VSP section below 60 ms, in the 40–80 m depth interval, a low-frequency – strong-amplitude down-going Stoneley wave can be seen. The Stoneley wave, generated in the borehole at the air-borehole fluid contact, is reflected at the top of karstic layers and strongly attenuated below.

The VSP was processed to separate the different wave fields. Figure 14 shows the extraction of the down-going Stoneley waves (Fig. 14a) and the up-going Stoneley waves (Fig. 14b).

The VSP sections clearly show the converted down-going and up-going Stoneley waves. The VSP sections are converted into instantaneous amplitude sections (Fig. 14a and b, central part). In each instantaneous amplitude VSP section, the instantaneous amplitudes of the Stoneley waves are stacked in a small corridor located after the arrival time of the down-going P-wave, to obtain body-wave to Stoneley-wave conversion factors (Fig. 14a and b, right part) used to detect the depth at which the conversion occurs (80–90 m depth interval).

During VSP acquisition, at each sensor (hydrophone) position, several records of ambient noise were registered. Figure 15a left, is an example of an ambient noise VSP section. The seismic noise was analyzed to detect the presence of flows (Mari & Porel, 2016). For this purpose, an ambient noise factor is calculated, which is defined as the average-to-standard deviation ratio of the amplitude spectrum of each noise trace. We noted a significant increase in the ambient noise factor at the level of karstic bodies. Ambient noise analysis therefore, shows that variations of the ambient noise factor correlate with the conversion level of P-waves into Stoneley waves (Fig.15a right).

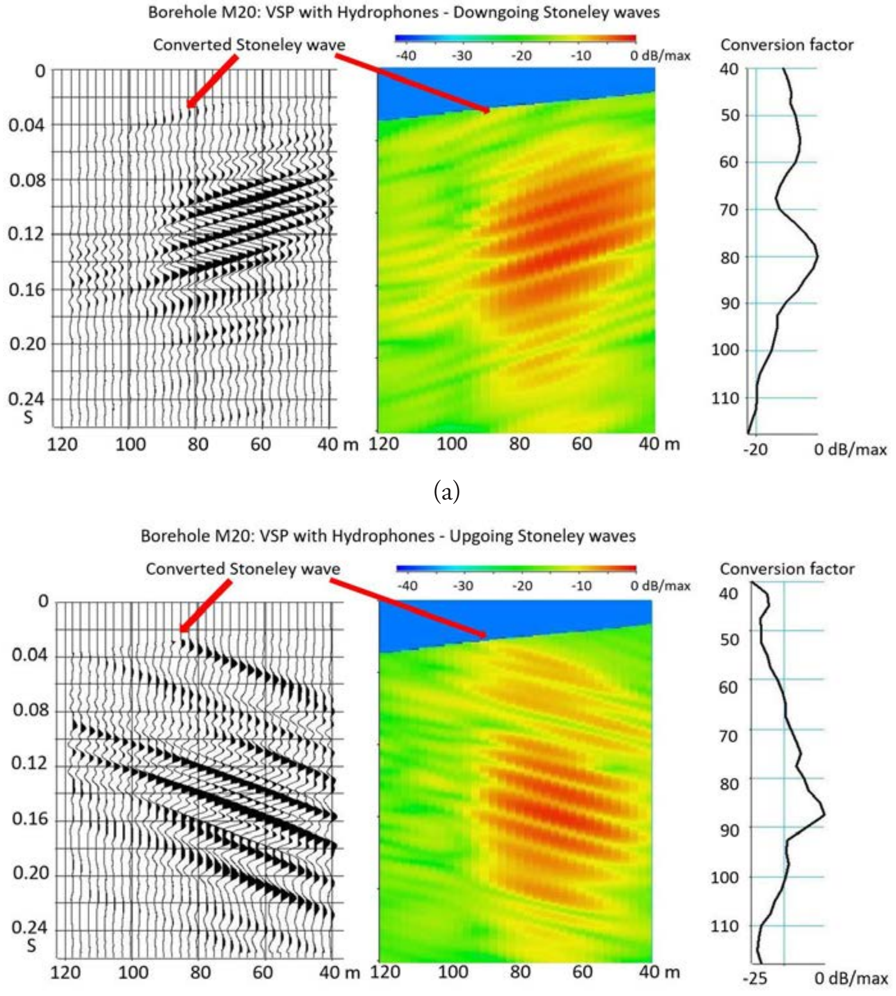

(a)

(b)

Figure 14 *Borehole M20: VSP with Hydrophones – Stoneley wave separations and conversion factor estimate. (a) Down-going Stoneley waves, (b) Up-going Stoneley waves.*

The attribute, called the VSP flow index, which is defined as the product of the ambient noise factor by the body-wave to Stoneley-wave conversion factor, was used to detect both karstic bodies and flow (Fig. 15b). In the same way as for the calculation of the acoustic flow log, a VSP flow rate is calculated from the VSP flow index.

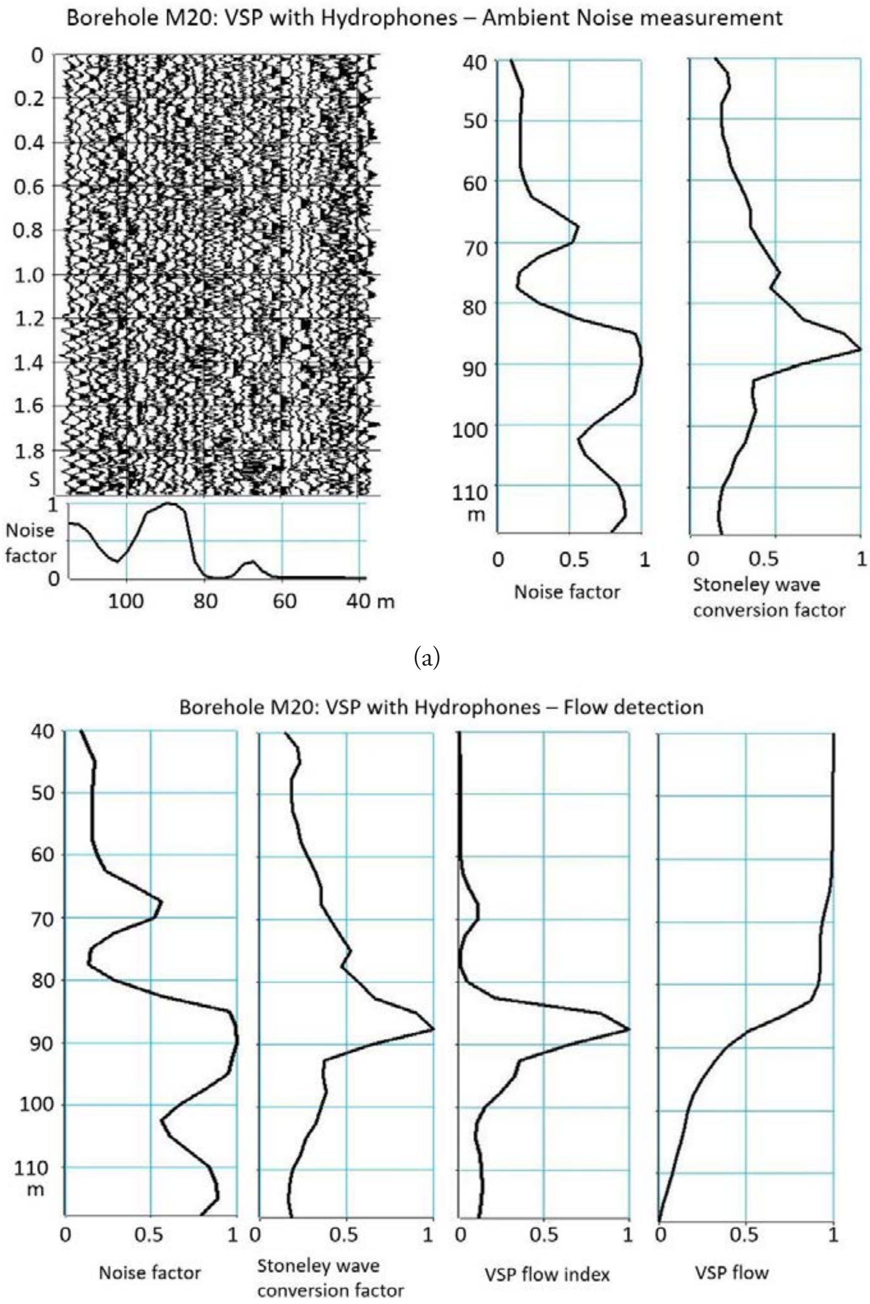

(a)

(b)

Figure 15 *Borehole M20: VSP with Hydrophones – ambient noise and flow detection estimate. (a) ambient noise, noise factor versus Stoneley wave conversion factor, (b) VSP logs and flow detection.*

5.5 Electrical methods

Electrical methods (Chapellier, 2001a) are extensively employed in near-surface geophysical investigations due to their sensitivity to subsurface resistivity contrasts. Surface-based techniques primarily include vertical electrical soundings (VES) and electrical profiling, implemented with various electrode configurations such as Wenner, Schlumberger, dipole-dipole, and pole-pole arrays. These configurations enable the investigation of both lateral and vertical resistivity variations (Loke & Barker, 1996a; Chapellier, 2001a).

Advanced 2D and 3D electrical resistivity imaging techniques have been developed to obtain spatially distributed resistivity models of the subsurface. These methods rely on the deployment of dense arrays of electrodes (often 48 to 256), connected via multicore cables, and positioned along linear or areal profiles. A computer-controlled multichannel resistivity meter sequentially selects electrode pairs for current injection and for measuring the resulting potential differences (ΔV), allowing for a large number of independent measurements in a single acquisition sequence.

Apparent resistivity values are computed for each measurement based on the known electrode geometry and are spatially referenced in terms of pseudo-depth (Z) and lateral position (X, Y). The resulting dataset is then processed using non-linear, iterative inversion algorithms that solve the governing equations of electrical conduction, typically using finite-element or finite-difference approaches (Loke & Barker, 1996b). The inversion reconstructs the true resistivity distribution within a 2D or 3D volume, subject to regularization constraints and starting from an initial a priori model.

This methodology, commonly referred to as Electrical Resistivity Tomography (ERT), is particularly effective for imaging complex geological structures, such as stratigraphic interfaces, fault zones, and karst features (Daily et al., 2004; Dahlin & Zhou, 2004; Torrese, 2020).

In addition to the 3D seismic survey, the HES was also analyzed using pseudo three-dimensional (3-D) Electrical Resistivity Tomography (ERT, https://doi.org/10.1016/j.jhydrol.2019.124257), where a 3-D model was constructed through the joint inversion of resistivity data acquired along parallel profiles (Torrese, 2020). The inverse resistivity model successfully identified the primary hydrogeological units, albeit with lower resolution compared to the 3D seismic survey. Modeling of synthetic datasets demonstrated the detectability of karst features through the pseudo 3-D ERT method. Furthermore, synthetic dataset modeling enabled the estimation of the experimental and inversion setup responses to varying levels of aquifer heterogeneity, utilizing well-log data and the 3D seismic block as geological prior information (Torrese, 2020).

In the context of borehole geophysics, conventional electric logging tools (Chapellier, 2001b) include laterolog and induction probes, which measure formation resistivity and conductivity over lateral investigation depths ranging from decimetric to several meters. These tools offer vertical resolutions of approximately 10–50 cm and are commonly used for lithological interpretation, fluid identification, and fracture detection (Ellis & Singer, 2007).

Electric logging tools — including single-point, short normal, and long normal logs (used to determine the resistivity Rt of the virgin zone) — were run in 12 wells: MP4, MP5, MP6, M11, M13, M14, M18, M21, M04, M07, M08, and M09. The Rt logs were used to estimate the formation porosity using Archie's law (Fig. 6 and 7). Figure 16 presents a comparison between the Rt logs and optical televiewer (OPTV) images for wells M04, M07, M08, and M11. The OPTV imagery confirms that zones of low resistivity correspond to open, water-filled karst conduits in the 85–90 m depth interval at boreholes M07, M08, and M11. A conductive horizon is identified on borehole M04, between 50.05 and 53.15 m depth, where a sequence of vertically stacked cavities up to 1 m in height is observed both on the OPTV log and on the long normal resistivity log (Fig. 16). This karstified interval corresponds to a bioturbated interval.

Figure 17 presents a comparison between the short normal (Rxo), caliper, and optical televiewer (OPTV) logs in borehole M07. The karst conduit in the 87–90 m depth interval is detected with a vertical resolution higher than that of the long normal resistivity (Rt) log. The caliper log provides very high vertical resolution and is particularly effective for detecting cavities and karst conduits. Unfortunately, at the SEH site, the caliper tool was run in only a limited number of boreholes.

The Electric Cylinder Method (ECM, Lantier and Frappin, 2000) represents an advanced borehole-based resistivity imaging technique. It involves the deployment of a flexible multi-conductor cable equipped with evenly spaced electrodes (spacing typically ranging from 0.3 m to 2 m) over a length of 9 to 60 meters. The cable is inserted into a borehole, and a programmable acquisition unit controls the selection of electrodes for current injections and potential measurements. A potential difference is established between a designated remote electrode (often outside the borehole) and an active current-injecting electrode along the cable. Multiple ΔV measurements are recorded between electrode pairs during each injection cycle, and the procedure is iterated for multiple injection positions along the cable. This configuration enables a quasi-volumetric acquisition within a cylindrical domain centered on the borehole axis. 3D inversion of the acquired dataset yields a high-resolution resistivity model within a radius of 2 to 20 meters around the borehole, depending on formation resistivity, electrode spacing, and inversion parameters (e.g., mesh density, regularization strength).

The ECM is particularly suited for the detection and characterization of subsurface heterogeneities (Frappin, 2011a) such as lithological discontinuities, fracture networks, altered or weathered zones, fault planes, karstic cavities, or anthropogenic voids (e.g., tunnels or buried structures). Its ability to provide continuous 3D imaging makes it a powerful complement to conventional borehole logging tools, especially in heterogeneous or anisotropic geological settings. The ECM is commonly used in geotechnical applications to measure the diameter of jet grouting columns (Frappin, 2011b).

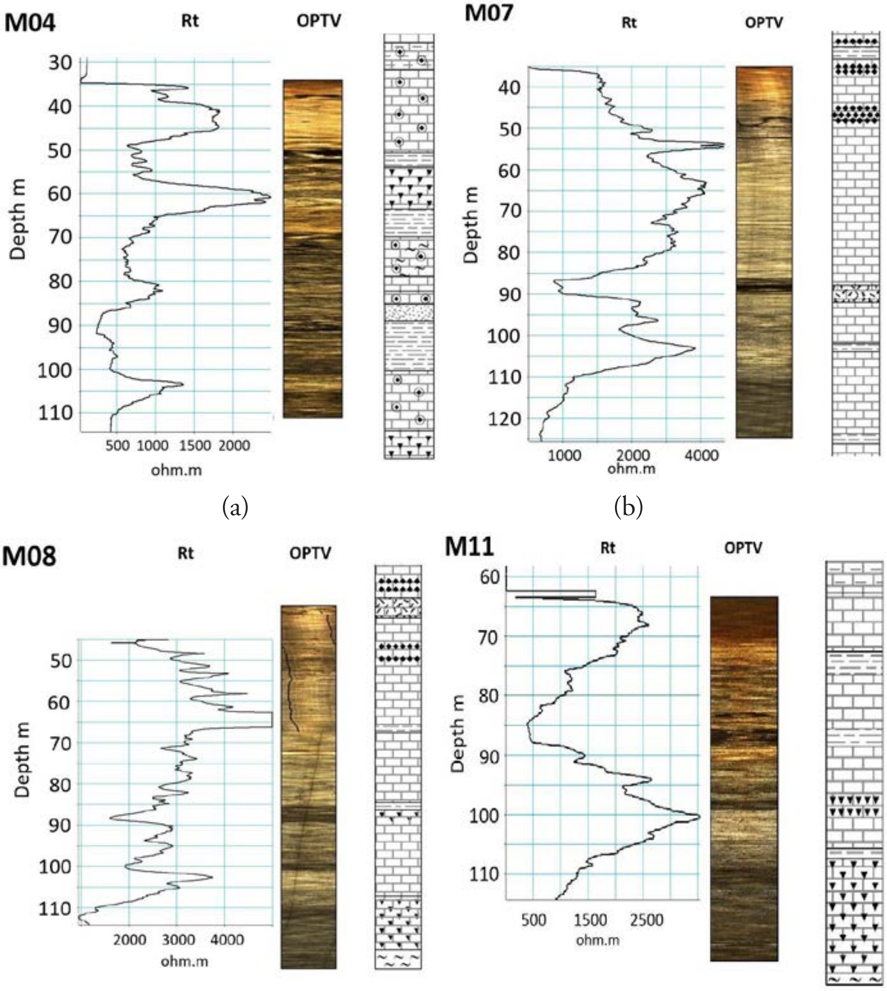

(a) (b)

(c) (d)

Figure 16 *Comparison of resistivity (Rt) logs and optical televiewer (OPTV) images in boreholes M04, M07, M08, and M11. On the OPTV images, dark zones — corresponding to low Rt values — indicate open, water-filled karst conduits in the 85–90 m depth interval in boreholes M07, M08, and M11.*

In addition to the 3D ERT method, the HES was also investigated using borehole electrical methods of the ERT type. The results are presented and discussed in Chapter 6, entitled *Borehole Electrical Panels: an experiment* (Moreau et al., 2026).

For example, the borehole electrical panels also detect the karst level identified through acoustic methods (Fig. 10 and 11) at a depth of 100 m in borehole M20 (Fig. 18). A comparison between the resistivity panels and optical wall imagery confirms that low-apparent resistivity anomalies correspond to open, water-filled karst conduits.

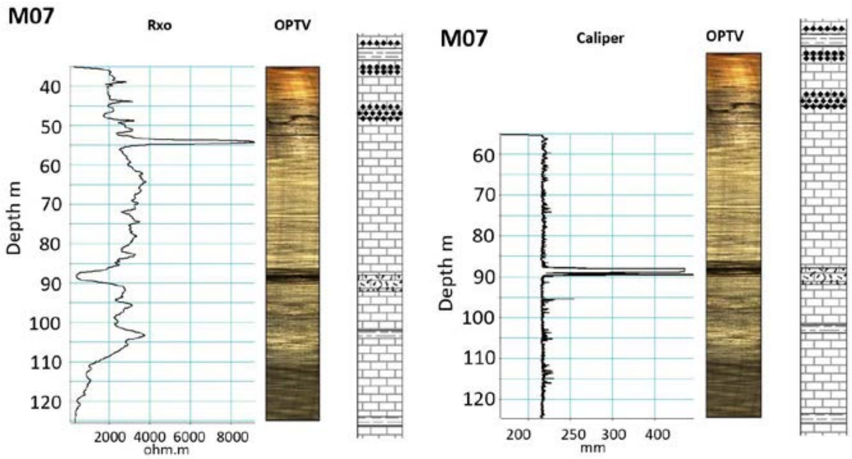

(a) (b)

Figure 17 *Comparison of the short normal resistivity (Rxo) log and borehole caliper with the optical televiewer (OPTV) image in borehole M07. The karst conduit is clearly identified in the 87–90 m depth interval.*

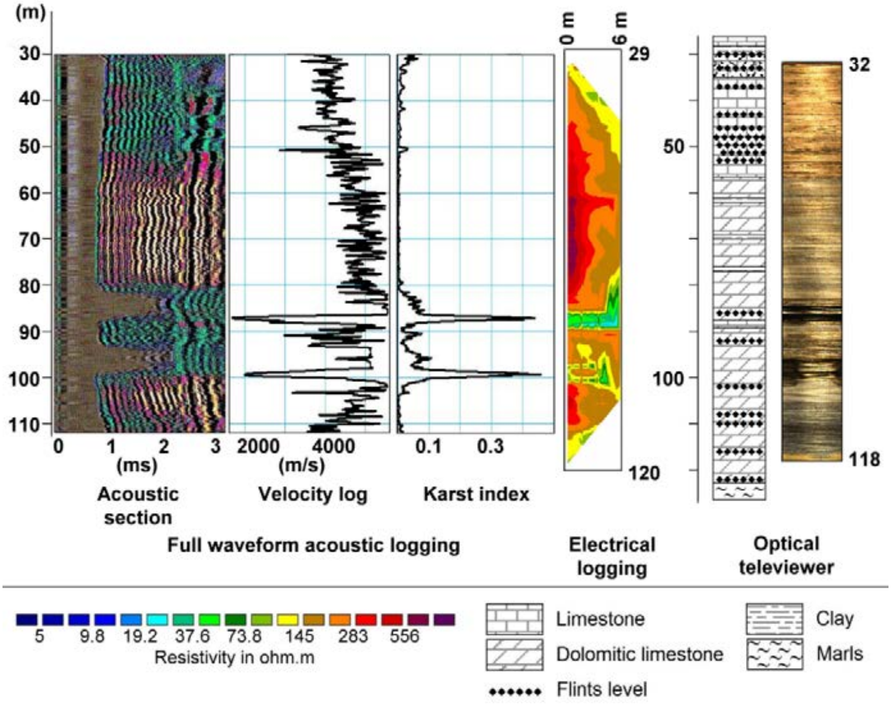

Figure 18 *Comparison of acoustic, electrical, and optical wall imaging methods in borehole M20. From left to right: acoustic section, velocity log, karst index log, electrical resistivity panel, geological log, and optical wall imagery (OPTV).*

5.6 Conclusions

The Hydrogeological Experimental Site (HES) of Poitiers, which was developed to conduct long-term monitoring and experiments on water and mass transfer processes, has been the site of hydrogeological and geophysical surveys as part of this study.

The chapter provides an overview of various field experiments based on seismic and acoustic methods and shows their relative contribution to knowledge of the experimental site.

A 3D seismic reflection and refraction survey was carried out. The 3D seismic data was processed to obtain both a structural model in depth (VSP data being used to define a time to depth conversion law), and the distribution of seismic velocities in the reservoir, using an inversion process with acoustic velocity logs as constraints. The result was a high-resolution 3D seismic block, with nearly horizontal stratification and strong lateral variations of velocity. This made it possible to identify three high-porosity, presumably water-producing layers, at depths of 35 to 40 m, 85 to 87 m, and 110 to 115 m. The 85 to 87 m deep layer is the most porous, with porosities of over 30%, which represents the karstic part of the reservoir.

To confirm the presence of karstic levels, borehole data were recorded in several boreholes in different frequency bandwidths. A methodology was developed to detect flow using both ambient noise measurement and VSP data. In low frequency band (10–150 Hz), VSP data were recorded with a hydrophone sensor, known to be sensitive to Stoneley waves that are currently used to detect discontinuities such as fractures or faults. Conversion of the down-going P-waves into Stoneley waves was observed at the level of the karstic bodies. This phenomenon occurs in highly permeable formations. Analysis of the ambient noise shows that variations of its characteristics (spectral variance) are correlated with the conversion level of P-waves into Stoneley waves. A VSP attribute, called VSP flow index, was calculated to detect both karstic levels and flows.

In high frequency bandwidth (1–20 kHz), full waveform acoustic data were recorded, both to locally validate the results obtained by the seismic methods (3D and VSP) and to evaluate the potential of the acoustic method to detect karstic bodies with a very high resolution. An acoustic attribute, called Karstic Index, was calculated to detect karstic levels.

Hydrogeological sites are currently investigated primarily by hydrogeological methods. In this study, we have shown how electrical logging (long normal logs), seismic and acoustic methods (3D seismic, full waveform acoustic logging, and VSP) can contribute to the understanding and description of karstic formations at different scales.

Both hydrogeological and geophysical investigations contribute to hydrogeological model building and site description. Figure 19 shows the benefit of combining the two types of investigation. The figure is a synthesis of the methods developed to detect karstic bodies and to quantify flows. The synthesis gathers data from acoustic logging (Karstic index), ambient seismic noise and VSP (VSP flow index), borehole wall imaging (OPTV optical televiewer) and flow measurement in dynamic conditions.

Combined analyses of geophysical and hydrogeological data can be done locally at wells or on a larger scale using 3D seismic data. These studies are done to detect water-producing levels in wells and to establish probable karst conduit networks. An integrated approach for the identification of effective three-dimensional (3D) discrete karst conduit networks conditioned on tracer tests and geophysical data (3D velocity block, Fig. 5a) has been developed (Bodin et al., 2022).

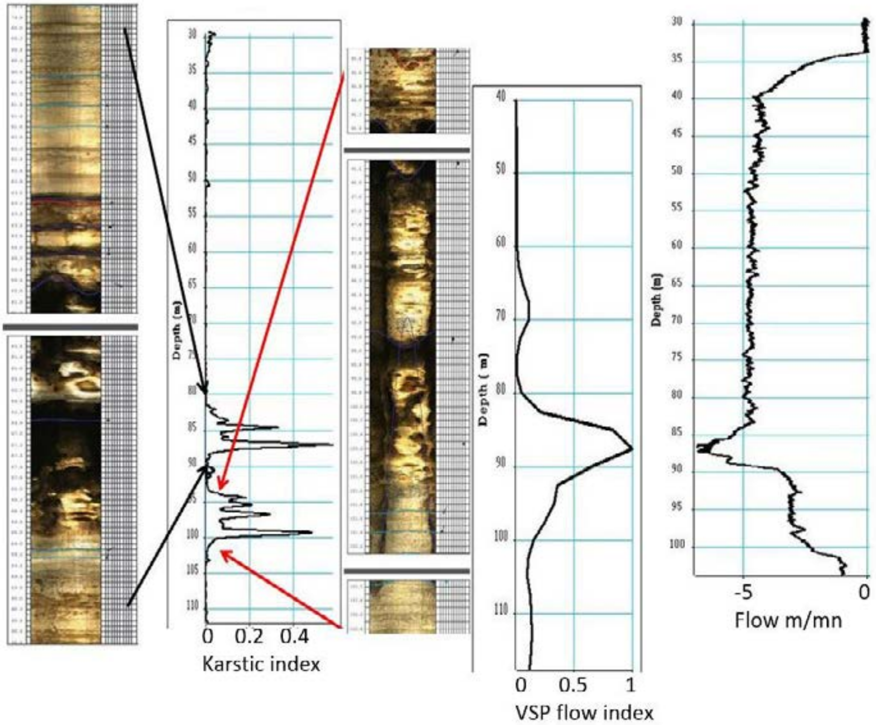

Figure 19 *Borehole M20: Detection of karstic levels and flows by acoustic logging (karstic index), VSP (VSP flow index), borehole wall imaging (OPTV) and flow measurement under dynamic conditions.*

Appendix: Static corrections

Refraction imaging of the subsurface is based on the analysis of refraction time-distance curves. The arrival time t(x) of the refracted wave is given by the following relationship:

$$t(x) = x.\cos(\alpha)/\ VR + \delta(0) + \delta(x)$$

- x: the source – receiver distance,
- α: the dip of refractor over the spread length,
- VR: the velocity of the refractor,
- $\delta(0)$: the delay time at the source point,
- $\delta(x)$: the delay time at the receiver point.

To accurately determine the true velocity, dip, and thickness of each subsurface marker, it is essential to obtain time-distance curves in both directions — i.e., up-dip and down-dip shooting. This requires seismic recordings where geophones are aligned with the shot points. The most widely known techniques for this are Hagedoorn's Plus-Minus method (1959) and the Generalized Reciprocal Method (GRM) introduced by Palmer (1986). The GRM is essentially an extension of the Plus-Minus method, and both rely on the concept of delay time. The Plus-Minus method is extensively used in seismic refraction surveying. Picked travel times are used to construct the t+ and t– curves. The t– curve provides the velocity of the refractor, while the t+ curve offers a time-based image of the refractor's depth (via delay times). If the velocity of the overlying medium is known, this delay curve can be converted into depth. This velocity is determined from the slope of the direct arrival. The overlying medium is referred to as the weathering zone (WZ). In the HES study area, the refractor velocity has been estimated at 3350 m/s based on t– curve interpretation, while the velocity of the weathering zone is approximately 850 m/s.

The arrival times of both direct and refracted waves were picked for all shots. These picked times serve as input data for applying Hagedoorn's Plus-Minus method. Cross-spread shots with a 60 m offset were also used to compute delay-time curves. These particular shots (Fig. 2d) were selected to ensure that the refracted wave is always the first arrival, regardless of the source–receiver distance.

For all shots — whether in-line or cross-line — the picked arrival times were carefully verified. This verification involved flattening the first arrival by applying the picked times as static corrections. Perfect flattening confirms accurate picking.

Picked times from in-line shots (Fig. 2b and 2c) and from 60 m cross-spread shots (Fig. 2b and 2d) were used to generate two delay-time maps.

The geostatistical processing applied to each delay-time map (Bourges et al., 2012) involved two main steps:

- detection of anomalous delay-time lines responsible for high spatial variability;
- kriging and extraction of long-wavelength structures, to reveal underlying geological features.

An initial variographic analysis was performed on both delay-time maps. The variograms were modeled using the following nested structures:

- in-line shot delay-time map: A cubic structure with a range of 50 m, consistent with the size of geological heterogeneities, and a spherical structure with a range of 140 m. The cross-line variogram revealed an additional source of variability attributed to acquisition artifacts, modeled by a spherical structure with a range of 10 m;
- cross-line shot delay-time map: A cubic structure with a range of 60 m, and an anisotropic spherical structure with ranges of 120 m in the in-line direction and 110 m in the cross-line direction.
  As with the in-line data, an additional variability source — attributed to acquisition artifacts — was modeled by a spherical structure with a range of 15 m.

Using the previously defined variogram models, both delay-time maps were interpolated. During this process, small-scale variability — associated with acquisition artifacts in the cross-line direction — was filtered out using factorial kriging. The interpolated maps were then compared to the original delay-time profiles. For the in-line shot survey, one anomalous acquisition line responsible for additional variability was identified, while two such lines were highlighted in the cross-line shot survey.

After removing the anomalous delay-time lines, omnidirectional variograms were computed, focusing on mid-scale variability (up to 50–70 m). For both delay-time maps, the updated variograms consist of:

- a cubic structure with a range of 49 m (in-line shots) and 60 m (cross-line shots), and
- a large-scale structure with a range of 120 m.

Finally, the two large-scale delay-time maps — representing long-wavelength geological features — were interpolated using factorial kriging. Given the high correlation between the two resulting maps (correlation coefficient ≈ 0.8), an average long-wavelength structure was computed.

The picked first-arrival times from all shots (both in-line and cross-line), the weathering zone (WZ) depth map derived from the averaged delay-time map (long-wavelength structure), and the velocity model obtained using the Plus–Minus method serve as input data for the inversion procedure — tomography — which is suitable for determining the subsurface velocity distribution (Mari and Mendes, 2012).

The velocity distribution obtained through the joint Plus-Minus tomographic inversion can be effectively used to compute 3D static corrections. For this purpose:

- the thickness H of the weathering zone is defined by the 2500 m/s iso-velocity depth map;
- the average velocity V_1 within the weathering zone is calculated from the velocity model in the 0 to H depth interval;
- the velocity V_2 of the refractor is derived from the velocity model within a narrow depth window (approximately 3 m) just below the interface at depth H.

The application of this methodology to the 3D dataset is illustrated in Figure A.1.

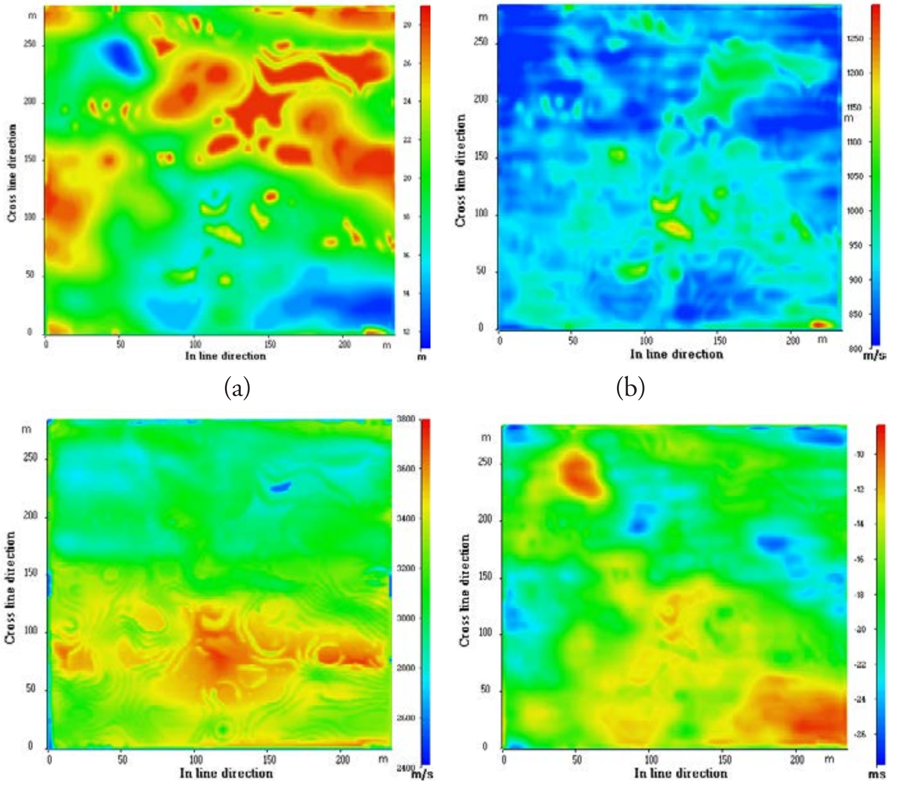

(a)

(b)

(c)

(d)

Figure A.1. *3D static corrections from 3D tomographic inversion after geostatistical processing. (a) Thickness H of the weathering zone. (b) Average velocity V1 in the weathering zone. (c) Velocity V2 below the weathering zone. (d) 3D static correction map (–H/V1 + H/V2).*

Acknowledgements

Special thanks to Matthieu Bourges for his help and expert advice in the geostatistical processing involved in computing 3D static corrections

References

Archie G.E. (1942). The electrical resistivity logs as an aid in determining some reservoir characteristics, *Petroleum Technology*, 146: 54-62.

Audouin O., Bodin J., Porel G., Bourbiaux B. (2008). Flowpath structure in a limestone aquifer: multi-borehole logging investigations at the hydrogeological experimental site of Poitiers, France, *Hydrogeology Journal*, 16(5): 939-950. https://doi.org/10.1007/s10040-008-0275-4

Binley A., Kemna A. (2005). DC resistivity and induced polarization methods. In Rubin, Y., & Hubbard, S. S. (Eds.), *Hydrogeophysics* (pp. 129-156). Springer.

Bodin J., Porel G., Nauleau B., Paquet D. (2022). Delineation of discrete conduit networks in karst aquifers via combined analysis of tracer tests and geophysical data, *Hydrol. Earth Syst. Sci.*, 26: 1713-1726, https://doi.org/10.5194/hess-26-1713-2022

Bourges M., Mari J.-L., Jeannee N. (2012). A practical review of geostatistical processing applied to geophysical data: methods and applications, *Geophysical prospecting,* 60: 400-412.

Chapellier D. (2001a). Electrical methods, from On-line course of geophysics (http://www-ig.unil.ch/)

Chapellier D. (2001b). Aquifer logging course, from On-line course of geophysics (http://www-ig.unil.ch/)

Dahlin T., Zhou B. (2004). A numerical comparison of 2D resistivity imaging with 10 electrode arrays. *Geophysical Prospecting*, 52(5): 379-398.

Daily W., Ramirez A., Binley A., La Brecque D. (2004). Electrical resistance tomography. *The Leading Edge*, 23(5): 438–442. https://doi.org/10.1190/1.1729225

Delay F., Mari J.-L., Porel G., Chabaux F., Ackerer P. (2022). Is subsurface geophysics as seismic and acoustic investigations a rescue to groundwater flow inversion? *Comptes Rendus Geoscience*, Part of Special Issue: Geo-hydrological data & models, https://doi.org/10.5802/crgeos.157

Ellis D.V., Singer J.M. (2007). *Well Logging for Earth Scientists* (2nd ed.). Springer.

Faust L.Y. (1953). A velocity function including lithologic variation, *Geophysics*, 18: 271-288.

Frappin P. (2011a). The electric cylinder. paper EG9, EAGE Conference & Exhibition, First International conference on Engineering Geophysics, 11-14 December 2011, AI Ain, United Arab Emirates.

Frappin P. (2011b). CYLJET: an innovative method for jet grouting column diameter measurement. paper EG44, EAGE Conference & Exhibition, First International conference on Engineering Geophysics, 11-14 December 2011, AI Ain, United Arab Emirates.

Gaudiani P. (1979). Système améliorant les procédés de mesures acoustiques, Brevet (Patent). 1979; 79 27528. Service des Brevets, 20 bis rue de Leningrad, 75800 Paris cedex 08.

Gaillard T., Moreau M., Mari J.-L. (2024). Seismic and stratigraphic characterization of karstogenic horizons in a sequence of carbonate deposits: Example of the Dogger limestones of the Poitou threshold, Journees Scientifiques AGAP Qualité 2024, *E3S Web of Conferences* 504, 05005, https://doi.org/10.1051/e3sconf/202450405005

Hagedoorn G.J. (1959). The Plus–Minus method of interpreting seismic refraction sections. *Geophysical Prospecting* 7: 158-182.

Lantier F., Frappin P. (2000). Method and apparatus for probing and inspecting an underground volume, patent EP 0 786 673 B1, deposit number: 97106066.0, European Patent office.

Loke M.H., Barker R.D. (1996a). Rapid least-squares inversion of apparent resistivity pseudo sections using a quasi-Newton method. *Geophysical Prospecting*, 44(1): 131–152. http://dx.doi.org/10.1111/j.1365-2478.1996.tb00142.x

Loke M.H., Barker R.D. (1996b). Practical techniques for 3D resistivity surveys and data inversion. *Geophysical Prospecting*, 44(3): 499–523. https://doi.org/10.1111/j.1365-2478.1996.tb00162.x

Mari J.-L., Porel G. (2008). 3D seismic imaging of a near – surface heterogeneous aquifer: a case study, *Oil and Gas Science and Technology*, *Rev. IFP*, 63: 179-201. https://doi.org/10.2516/ogst:2007077

Mari J.-L., Porel G., Bourbiaux B. (2009). From 3D seismic to 3D reservoir deterministic model thanks to logging data: the case study of a near – surface heterogeneous aquifer, *Oil and Gas Science and Technology, Rev. IFP,* 64: 119-131. https://doi.org/10.2516/ogst/2008049

Mari J.-L., Delay F. (2011). Contribution of Seismic and acoustic methods to reservoir model building, in "Hydraulic Conductivity / Book 1", *In Tech, Open Access Publisher*, ISBN 978-953-307-288-3, https://doi.org/10.5772/22051

Mari J.-L., Mendes M. (2012). High resolution near surface imaging of fracture corridors and cavities by combining Plus Minus method and refraction tomography. *Near Surface Geophysics*, 10: 185-195. https://doi.org/10.3997/1873-0604.2011052

Mari J.-L., Porel G. (2015). Automated karstic reservoir analysis utilizing attributes, We N117 02, 77th EAGE Conference & Exhibition, Madrid IFEMA, Spain.

Mari J.-L., Porel, G. (2016). Flow detection using well seismic data, Tu P2 02, 78th EAGE Conference & Exhibition, Vienna, Austria, 30 May-2 June.

Mari J.-L., Porel G. (2018). “Contribution of seismic and acoustic methods to the characterisation of karstic formations”, Chapter 5 in *Well seismic surveying and acoustic logging*, EDP Sciences. https://doi.org/10.1051/978-2-7598-2263-8

Mari J.-L., Mendes M. (2019). *Seismic imaging: a practical approach*, EDP Sciences. https://doi.org/10.1051/978-2-7598-2351-2

Mari J.-L., Porel G., Delay F. (2020). Contribution of Full Wave Acoustic Logging to the Detection and Prediction of Karstic Bodies. *Water,* 12(4): 948. https://doi.org/10.3390/w12040948

Mari J.-L., Porel G. (2024). The hydrogeological experimental site of Poitiers: Hydrogeological versus geophysical investigations, Journees Scientifiques AGAP Qualité 2024, *E3S Web of Conferences* 504: 05003. https://doi.org/10.1051/e3sconf/202450405003

Moreau M., Brunel P., Mari J.-L. (2026). “Borehole electrical panels: an experiment”, Chapter 6 in *A new concept of karst development based on hydrogeology and geophysics*, EDP Sciences. https://doi.org/10.1051/978-2-7598-3934-6.c006

Palmer D. (1986). Refraction seismic, *Geophysical Press*, 13.

Torrese P. (2020). Investigating karst aquifers: using pseudo 3-D electrical resistivity tomography to identify major karsts features, *Journal of Hydrology*, 580(2): 124257. https://doi.org/10.1016/j.jhydrol.2019.124257